Numeric Validation of the Inversion Model of Electrical Resistivity Imaging Method using the Levenberg-Marquardt Algorithm

Tuan Anh Nguyen
STASD Research Group, Ho Chi Minh City University of Transport, Vietnam
tuananh.nguyen@ut.edu.vn

Received: 5 December 2023 | Revised: 16 December 2023 | Accepted: 20 December 2023

Licensed under a CC-BY 4.0 license | Copyright (c) by the authors | *https://doi.org/10.48084/etasr.6705*

ABSTRACT

This paper introduces a new application of the Electrical Resistivity Imaging (ERI) method within the realm of structural assessment, deviating from its conventional use in geology. The study presents an innovative inversion model that incorporates the Levenberg-Marquardt algorithm, representing a notable leap in seamlessly integrating ERI into structural analysis. Rigorous validation of the inversion methodology is conducted through extensive benchmarking against simulated reference data, focusing on 1D and 2D resistivity distributions within timber specimens. By utilizing known resistivity fields, the paper quantitatively validates the accuracy of reconstructed models obtained through numerical simulations. Notably, both longitudinal and transverse surveys exhibit exceptional outcomes, showcasing a high correlation with the actual resistivity profiles, achieved within a concise 10-13 iterations. This meticulous validation process conclusively underscores the effectiveness and precision of the proposed inversion approach. Beyond its scientific contribution, this research expands the conventional boundaries of ERI application and establishes it as an invaluable tool for structural monitoring.

Keywords-ERI; inversion model; resistivity; Levenberg-Marquardt; numeric validation

I. INTRODUCTION

Electrical Resistivity Imaging (ERI) is a highly effective geophysical technique employed for mapping subsurface variations in both lateral and vertical electrical resistivity [1-3]. This method involves deploying arrays of electrodes on the ground surface to inject current and measure potential differences within the subsurface. The systematic arrangement of electrodes in the ground is crucial for the subsurface resistivity assessment. The measurement process involves applying a precisely measured direct current or low-frequency alternating current (denoted as I_{AB}) between electrodes A and B. Subsequently, the voltage of the alternating current (denoted as ΔV_{MN}) is measured between the remaining electrodes M and N, which serve as potential electrodes. Apparent resistivity data collected along survey lines are processed and inverted to produce 2D and 3D models of true resistivity distribution. ERI has wide applicability for near surface investigations related to civil infrastructure, hydrogeology, environmental assessment, and archeology due to its ability to differentiate materials based on electrical properties. Factors such as mineral composition, porosity, water content, and salt concentration influence field measurements [4, 5]. By detecting electrical property contrasts, ERI can delineate subsurface lithological contacts, solution cavities, contaminant plumes, and structural features without cumbersome drilling [2, 6]. ERI is also employed for structural health monitoring of concrete and timber elements. Variations in moisture content, cracks, and defects create contrasts in electrical conductivity that are mapped through inversion of the resistivity data. This allows accurate identification of internal damage in concrete caused by corrosion, leakage, or erosion [7, 8]. For timber, ERI enables differentiation of moisture gradients and decay pockets based on resistivity contrasts without extensive drilling [9]. The sensitivity of ERI to subtle changes in electrical properties allows early detection of latent defects and deterioration prior to visual manifestations on the structural.

In geophysics, the Res2Dinv software facilitates the computation of the projected resistivity field onto the study area using apparent resistivity values measured in the field [6, 10]. This calculation relies on an inverse method that minimizes the difference between experimental measurements and apparent resistivities derived from numerical computations. The underlying principle, termed inversion, assumes point injection into a semi-infinite medium, which is notably unrealistic in this context due to the limited and confined structural dimensions in space. This paper develops an inversion model that allows for considering the actual geometry of the studied volumes.

II. THE LEVENBERG-MARQUARDT ALGORITHM AND ITS APPLICATION TO THE ELECTRICAL RESISTIVITY OPTIMIZATION PROBLEM

Levenberg-Marquardt is an effective algorithm for nonlinear regression models [11-13]. It strategically combines

Gradient Descent [14, 15] and Gauss-Newton approaches [16, 17]. When parameters are distant from the optimal values, the algorithm leverages a Gradient Descent-like search to approach global optimum territory while avoiding entrapment in suboptimal local extrema. As the solution trajectory nears putative optima, the technique transitions to exploit Gauss-Newton's rapid fine-scale convergence properties. This blended approach confers multiple advantages over pure Gradient Descent. By prioritizing global exploration initially, Levenberg-Marquardt avoids stagnation in local minima. The subsequent activation of Gauss-Newton's efficient local search allows precision-tuning of parameters to expedite convergence at optimized coordinates. However, disadvantages include substantially greater computational overhead versus basic Gradient Descent, as well as more intricate algorithmic implementation. $d = \{d_1, d_2, ..., d_N\}$ represents the measured data (with N being the number of measurements), and $m = \{m_1, m_2, ..., m_M\}$ represents the model parameters (with M being the number of parameters). So, the model function is: $f = f(m)$.

According to the least squares method, the expression of the difference between measured and calculated data, or also referred to as the objective function F is then expressed in the following matrix form:

$$F = (\Delta d - J\Delta m)^T . (\Delta d - J\Delta m) \quad (1)$$

In this context, Δd denotes the variance between the measured and computed data. The inversion outcomes converge towards adjusting the initial model m_0 through a correction Δm.

$$\Delta d = d - f(m_0) \quad (2)$$

$$\Delta m = m - m_0 \quad (3)$$

The Jacobian matrix encodes localized gradient information to guide optimization algorithms towards minimizing model-data misfit. Its size matches observations by parameters, with elements quantifying parameter influence on each data point. For nonlinear inverse problems, iterative methods successively update parameters along the Jacobian-indicated descent direction.

$$J_{ij} = \frac{\partial f(m_i)}{m_j} \quad (4)$$

The correction vector is thus defined by:

$$\Delta m = \left(J^T J + \lambda W_m\right)^{-1} J^T \Delta d \quad (5)$$

The damping parameter λ enables regularization of the approximation to the Hessian matrix $J^T J$ utilized during inversion, mitigating ill-conditioning via addition of a scalar value to the eigenvalues. Conceptually, λ mediates the tradeoff between resolution and accuracy in the inverse problem solution. Excessive damping magnitudes prolong inversion execution. However, the resultant models can demonstrate improved fidelity. Conversely, reduced λ values prioritize efficient convergence over precision. Accordingly, common Levenberg-Marquardt implementations allow dynamic tuning of λ: decreasing the damping factor when the objective function shows decreasing misfit to accelerate mapping, while increasing λ to restore stabilization upon divergence. The modulated attenuation introduced by the damping parameter therefore facilitates adaptive control over convergence and precision. Further analysis of automated, data-driven λ selection is warranted to optimize the balance between model accuracy and computational efficiency.

In the electrical inversion problem, the vector *m* is defined as the conductivity, and the resistivity is determined as the reciprocal of *m*.

$$m_{resistivity} = \left\{\frac{1}{m_1}, \frac{1}{m_2}, ..., \frac{1}{m_M}\right\} \quad (6)$$

The key to the inverse problem lies in the selection of M. A larger value of M leads to a more accurate electrical resistivity field, however, an increase in M may render the inverse problem resource-intensive and potentially unsolvable. Therefore, this paper proposes dividing the sample into M elements with constant electrical resistivity within each element. The vector *m* comprises components that represent the conductivity values of the M elements. The measured $\frac{\Delta V_{MN}}{I_{AB}}$ can be represented in the form of a vector *d* which is called the measured data vector. *N* represents the number of measurements dictated by the multiplexing. The direct problem is then defined as a function *f(m)* whose result is expressed in the form of a vector composed of the $\frac{\Delta V_{MN}}{I_{AB}}$ values computed by the direct model.

III. NUMERIC VALIDATION OF THE INVERSION MODEL

A. Details of the Numerical Inversion Validation Process

1) Initial Resistivity Model

An initial homogeneous resistivity model m_0 is defined, with a value reasonably approximating known subsurface conditions.

2) Parameterization

The model domain is discretized into M elements of homogeneous resistivity values to be estimated through inversion.

3) Forward Modeling

For a given *m*, the numerical direct model predicts the array voltage response $\frac{\Delta V_{MN}}{I_{AB}}$. An accurate simulation of the true subsurface electric field is required.

4) Inversion

An iterative optimization algorithm adjusts the resistivity model to minimize the misfit between measured and modeled $\frac{\Delta V_{MN}}{I_{AB}}$, generating a correction vector d at each iteration based on the Levenberg-Marquardt method.

5) Convergence

Inversion terminates once predefined stopping criteria are met relating model parameters, misfit error, and number of iterations. If convergence fails, regularization parameters and discretization can be adjusted. Final modeled resistivities comprise the inverted section. The validation process for the inversion model involves utilizing data resolved by the direct model, which are subsequently introduced into the inverse model as "measured data". Knowledge of the true resistivity field permits the validation of the inversion model. This article builds upon the direct finite element model developed in [9] which enables simulating the multiplexed measurement algorithm coupling the resolution of Ohm's law (current injection and electric potential calculation) with a multiplexing procedure concordant with the measurement configuration. For any given resistivity field, the model can determine the numerical values of $\frac{\Delta V_{MN}}{I_{AB}}$ when measured with different multiplexers. The validation of the inversion model is carried out in two cases: (1) Longitudinal resistivity profile and (2) traverse resistivity profile.

B. Case 1: Longitudinal Resistivity Profile

This problem is based on the assumption of a homogeneous resistivity distribution on the traverse section. Consider a timber specimen with dimensions of 320 × 95 × 95 mm^3 and 21 inline electrodes spaced by 15 mm in an array along the length of the specimen as shown in Figure 1. Cylindrical metal electrodes with a diameter of 2 mm are inserted into the sample to a depth of 10 mm.

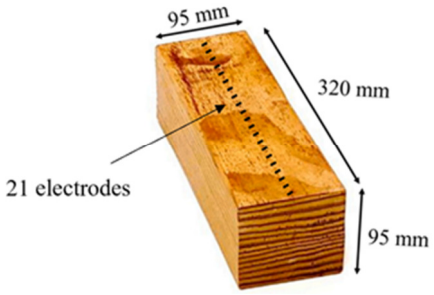

Fig. 1. Dimensions of the specimen and electrode arrangement for the case 1 model.

This study uses a dipole-dipole quadrupole configuration, which allows obtaining a very low electromagnetic coupling between the current and potential lines while giving a high density of measurement points (Figure 2). Consider a resistivity field with a gradient shape varying from 10^4 to 10^6 Ωm as shown in Figure 3.

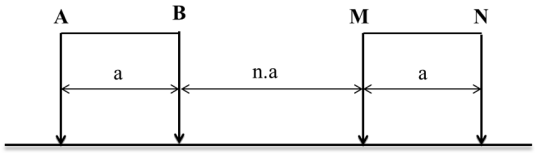

Fig. 2. Dipole - dipole configuration.

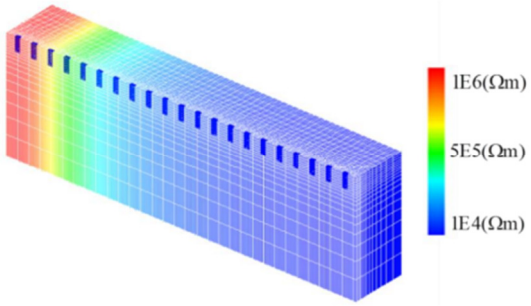

Fig. 3. The electrical resistivity field of case 1 into the direct model.

The current injection in forward modeling is simulated using three types of dipole-dipole quadrupole arrays by varying the n values successively to n = 1 (type 1), n = 2 (type 2), and n = 3 (type 3), allowing for the determination of a total of 51 numeric values of $\frac{\Delta V_{MN}}{I_{AB}}$. These 51 values are used as the "measured data" fed into the inverse model to determine the resistivity field of the specimen. In this case, the known resistivity field beforehand allows validating the accuracy of the inversion model.

C. Case 2: Traverse Resistivity Profile

The specimen is a cubic prism with dimensions of 95 × 95 × 95 mm^3. In this case, the approach is generalized to an electrode arrangement in the form of a belt. Five electrodes per face are spaced 15 mm apart, in a two-dimensional configuration (Figure 4). In contrast to the previous one-dimensional case, all quadrupole configurations are exploited. This makes it possible to investigate the entire cross-section and achieve a high density of measurement points, not only on the surface but also inside the core. Two multiplexing processes are implemented per measurement: Multiplexing 1 sweeps electrodes 1 through 20, multiplexing 2 sweeps electrodes 10 to 11 (Figure 5).

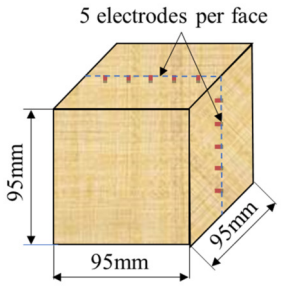

Fig. 4. Dimensions of the specimen and electrode arrangement for the case 2 model.

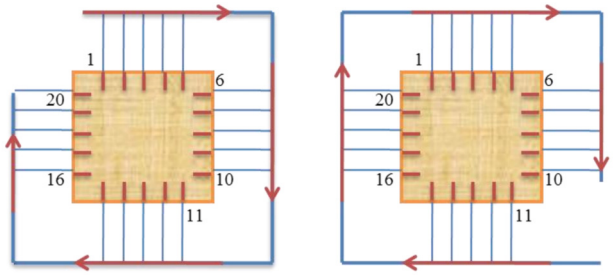

Fig. 5. Two electrical measurement directions of case 2 specimen.

The goal is to determine the resistivity distribution in a cross-section of the sample. The hypothesis of constant resistivity, along the longitudinal direction, is then proposed. Similar to the longitudinal case, we consider an example of an exponentially varying resistivity profile from 10^4 to 10^6 Ωm as shown in Figure 6.

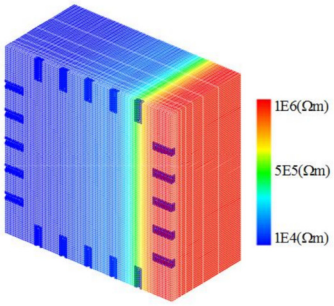

Fig. 6. The electrical resistivity field of case 2 into the direct model.

Multiplexing (Figure 5) produces 319 values of $\frac{\Delta V_{MN}}{I_{AB}}$. These values are used as the "measured data" fed into the inverse model to determine the resistivity field of the specimen.

D. The Inverse Problem-solving Process

In Case 1, the sample is segmented into 10 equal-length segments, while in Case 2, it is discretized into a grid of 5×5 elements. Each segment in Case 1 and each element in Case 2 is characterized by a homogeneous resistivity value (Figure 7).

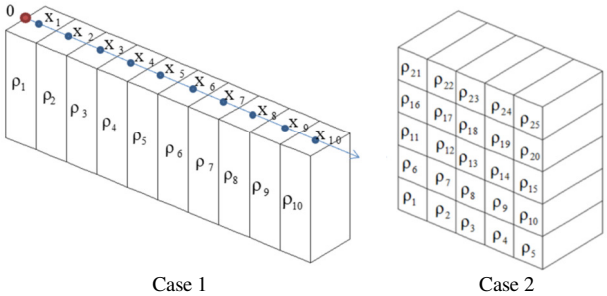

Fig. 7. Coarse meshing for the implementation of the inversion model.

Let us choose the initial condition m_0 as a homogeneous electrical resistivity of 10^7 Ωm. Since the function f_m is essentially the direct model, the values of the Jacobian matrix cannot be directly computed through differentiation. Therefore, an approximate calculation method is proposed:

$$J_{ij} = \frac{f_i(m_j + \Delta m_j) - f_i(m_j)}{\Delta m_i} \quad (7)$$

The regularization parameter λ is dynamically selected during the inversion process. The first iteration starts with a sufficiently high λ_0 value relative to the Jacobian matrix terms, to ensure stability. For subsequent iterations, λ is updated based on the change in objective function: it is reduced by a factor α if the objective function decreases (indicating convergence) or increased by a factor β otherwise. Direct matrix inversion utilizes partial pivoting Gaussian factorization. The stopping criterion is based on the parameter variation between two successive iteration i+1 and i falls below a threshold f_m, as defined in (8):

$$\left|\frac{m_{i+1} - m_i}{m_i}\right| \le f_m \quad (8)$$

In this case, we choose $\lambda_0 = 10^{16}$, α = 0.1, and β = 10, with the stopping criterion set to $f_m = 10^{-3}$.

For Case 1, the time required for each iteration is less than 15 min. The inversion procedure stops after 12 iterations. The mean absolute discrepancy between measured and inverted $\frac{\Delta V_{MN}}{I_{AB}}$ values is 6.8%. By comparing the differences between measured and inverted $\frac{\Delta V_{MN}}{I_{AB}}$, in the bulk region, the inversion yields promising results, however, near the sample edges, where the current lines are constrained, the algorithm lacks efficiency (Figure 8). Ultimately, the mesh density has to be compatible with the richness of information - sparser towards the edges compared to the central region.

The thickness of the two segments at the edges is selected as 4 cm, while the bulk region is discretized into 8 segments with equal thickness values of 3cm (Figure 9).

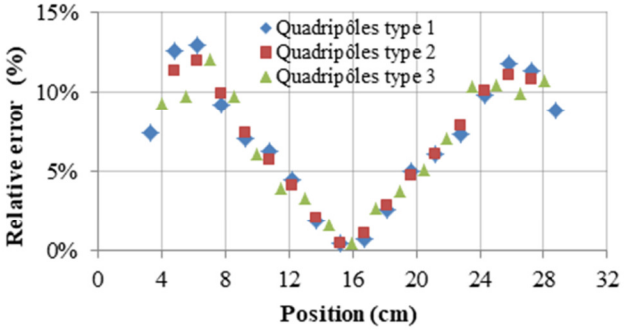

Fig. 8. Relative error between measured and estimated $\frac{\Delta V_{MN}}{I_{AB}}$ resulting from the Case 1 discretization into 10 qual-thickness segments.

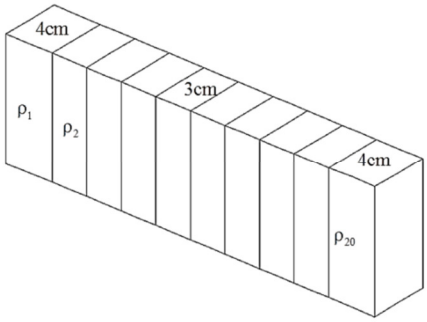

Fig. 9. Coarse meshing of the Case 1 specimen with unequal-thickness segments.

The inversion procedure terminates after 10 iterations. The inverted resistivity model exhibits a commendable correlation with the true resistivity distribution, as confirmed by a small deviation (0.05%) between the measured and predicted $\frac{\Delta V_{MN}}{I_{AB}}$ responses (Figure 10). Thus, it can be observed that employing a grid division aligned with the measured density region enables the determination of the corresponding appropriate electrical resistivity field.

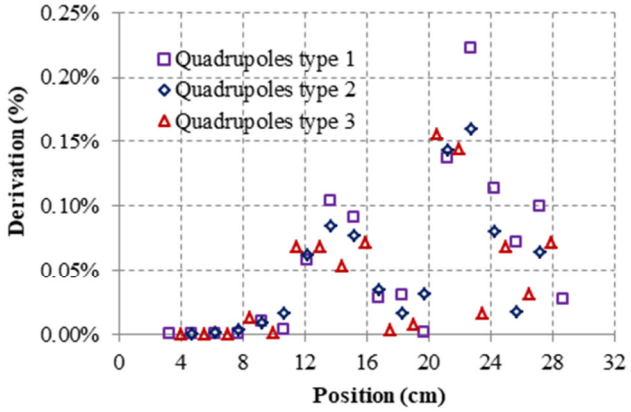

Fig. 10. Relative error between measured and estimated $\frac{\Delta V_{MN}}{I_{AB}}$ resulting from the Case 1 discretization into 10 inequal-thickness segments.

For Case 2, each iteration takes 55 min with the inversion stopping at the 12th iteration. The difference between the measured and estimated $\frac{\Delta V_{MN}}{I_{AB}}$ is less than 0.5% on average. Figure 11 indicates that the errors of the 3 types of dipole-dipole and quadrupole configurations are smaller than those of the remaining quadrupoles.

Through the two considered examples, it can be concluded that the inverse model constructed using the Levenberg-Marquardt algorithm was able provide reliable results.

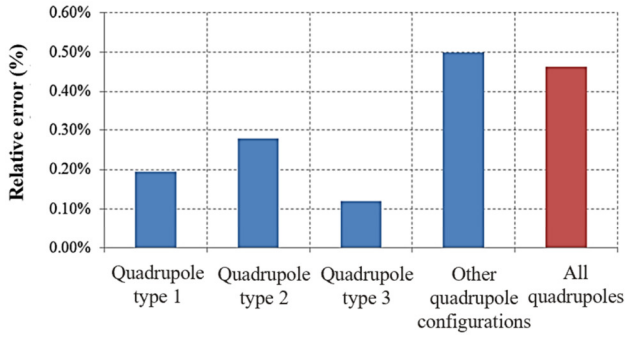

Fig. 11. Relative error between measured and estimated $\frac{\Delta V_{MN}}{I_{AB}}$ resulting from the Case 2 resolution.

IV. CONCLUSION

In conclusion, this paper presented a method of employing the Levenberg-Marquardt algorithm for electricity resistivity inversion. The article proposed a strategy for selecting the lambda coefficient based on the magnitude of the Jacobian matrix, with the additional adjustment of increasing or decreasing coefficients by a factor of 10 to ensure algorithm convergence and efficient problem-solving. The paper also outlined an approximate method for calculating the Jacobian matrix since computing derivatives becomes impractical when utilizing the direct model as the model function.

Furthermore, the development of the inverse model and its validation were elucidated, utilizing numerical data from the direct model as simulated measurement values. This validation approach involves comparing the obtained results with pre-known resistivity field values, affirming the accuracy of the inverse model. Applying the inversion algorithm to map resistivity distributions in timber specimens, specifically addressing 1D and 2D resistivity profiles (longitudinal and traverse), has showcased the accuracy of the inverse model. After 10-13 iterations, the inverse model yielded results with an error below 1% for both cases, thus confirming the effectiveness of the inversion approach.

While these 1D and 2D examples show promising outcomes for the inversion algorithm, integrating real-world experimental data into the validation phase is crucial for reinforcing the robustness and reliability of the proposed method. Further experimentation and verification in actual field conditions are essential steps to validate the practical applicability of the presented approach.

REFERENCES

[1] M. H. Loke, J. E. Chambers, D. F. Rucker, O. Kuras, and P. B. Wilkinson, "Recent developments in the direct-current geoelectrical imaging method," *Journal of Applied Geophysics*, vol. 95, pp. 135–156, Aug. 2013, https://doi.org/10.1016/j.jappgeo.2013.02.017.

[2] O. O. Osinowo and M. O. Falufosi, "3D Electrical Resistivity Imaging (ERI) for subsurface evaluation in pre-engineering construction site investigation," *NRIAG Journal of Astronomy and Geophysics*, vol. 7, no. 2, pp. 309–317, Dec. 2018, https://doi.org/10.1016/j.nrjag.2018.07.001.

[3] C. Ungureanu, A. Priceputu, A. L. Bugea, and A. Chirică, "Use of electric resistivity tomography (ERT) for detecting underground voids on highly anthropized urban construction sites," *Procedia Engineering*,

vol. 209, pp. 202–209, Jan. 2017, https://doi.org/10.1016/j.proeng. 2017.11.148.

[4] S. Soto-Caban and E. Law, "Using Resistivity Measurements to Determine Anisotropy in Soil and Weathered Rock," *Engineering, Technology & Applied Science Research*, vol. 3, no. 4, pp. 483–487, Aug. 2013, https://doi.org/10.48084/etasr.368.

[5] G. S. Solangi, A. A. Siyal, M. M. Babar, and P. Siyal, "Spatial Analysis of Soil Salinity in the Indus River Delta, Pakistan," *Engineering, Technology & Applied Science Research*, vol. 9, no. 3, pp. 4271–4275, Jun. 2019, https://doi.org/10.48084/etasr.2818.

[6] J. D. Ducut *et al.*, "A Review of Electrical Resistivity Tomography Applications in Underground Imaging and Object Detection," *Displays*, vol. 73, Jul. 2022, Art. no. 102208, https://doi.org/10.1016/j.displa. 2022.102208.

[7] J. F. Lataste, C. Sirieix, D. Breysse, and M. Frappa, "Electrical resistivity measurement applied to cracking assessment on reinforced concrete structures in civil engineering," *NDT & E International*, vol. 36, no. 6, pp. 383–394, Sep. 2003, https://doi.org/10.1016/S0963-8695(03)00013-6.

[8] K. Karhunen, A. Seppänen, A. Lehikoinen, P. J. M. Monteiro, and J. P. Kaipio, "Electrical Resistance Tomography imaging of concrete," *Cement and Concrete Research*, vol. 40, no. 1, pp. 137–145, Jan. 2010, https://doi.org/10.1016/j.cemconres.2009.08.023.

[9] T. A. Nguyen, "Approches expérimentales et numériques pour l'étude des transferts hygroscopiques dans le bois," Ph.D. dissertation, Université de Limoges, Limoges, France, 2014.

[10] S. F. Yasir, J. Jani, and M. Mukri, "A dataset of visualization methods to assessing soil profile using RES2DINV and VOXLER software," *Data in Brief*, vol. 24, Jun. 2019, Art. no. 103821, https://doi.org/ 10.1016/j.dib.2019.103821.

[11] A. Kleefeld and M. Reißel, "The Levenberg–Marquardt method applied to a parameter estimation problem arising from electrical resistivity tomography," *Applied Mathematics and Computation*, vol. 217, no. 9, pp. 4490–4501, Jan. 2011, https://doi.org/10.1016/j.amc.2010.10.052.

[12] X. Wang, P. Wang, X. Zhang, Y. Wan, W. Liu, and H. Shi, "Efficient and robust Levenberg–Marquardt Algorithm based on damping parameters for parameter inversion in underground metal target detection," *Computers & Geosciences*, vol. 176, Jul. 2023, Art. no. 105354, https://doi.org/10.1016/j.cageo.2023.105354.

[13] T. Dridi, H. Jouini, A. Mami, A. E. Mhamedi, and E. M. Dafaoui, "Application of the Levenberg-Marquardt Algorithm in Solving the Economic Emission Dispatch Problem Integrating Renewable Energy," *Engineering, Technology & Applied Science Research*, vol. 12, no. 4, pp. 8850–8855, Aug. 2022, https://doi.org/10.48084/etasr.5002.

[14] A. Lemita, S. Boulahbel, and S. Kahla, "Gradient Descent Optimization Control of an Activated Sludge Process based on Radial Basis Function Neural Network," *Engineering, Technology & Applied Science Research*, vol. 10, no. 4, pp. 6080–6086, Aug. 2020, https://doi.org/ 10.48084/etasr.3714.

[15] G. Tomasi and R. Bro, "2.22 - Multilinear Models: Iterative Methods," in *Comprehensive Chemometrics*, S. D. Brown, R. Tauler, and B. Walczak, Eds. Oxford: Elsevier, 2009, pp. 411–451, https://doi.org/ 10.1016/B978-044452701-1.00053-3.

[16] D. Constales, G. S. Yablonsky, D. R. D'hooge, J. W. Thybaut, and G. B. Marin, "Chapter 9 - Experimental Data Analysis: Data Processing and Regression," in *Advanced Data Analysis & Modelling in Chemical Engineering*, D. Constales, G. S. Yablonsky, D. R. D'hooge, J. W. Thybaut, and G. B. Marin, Eds. Amsterdam, Netherlands: Elsevier, 2017, pp. 285–306, https://doi.org/10.1016/B978-0-444-59485-3.00009-6.

[17] M. Meloun and J. Militký, "8 - Nonlinear Regression Models," in *Statistical Data Analysis*, M. Meloun and J. Militký, Eds. Woodhead Publishing India, 2011, pp. 667–762, https://doi.org/10.1533/ 9780857097200.667.